



Spatial analysis of ambient gamma dose equivalent rate data by means of digital image processing techniques



Katalin Zsuzsanna Szabó ^{a, *}, Gyozo Jordan ^a, Attila Petrik ^b, Ákos Horváth ^c, Csaba Szabó ^d

^a Department of Chemistry, Institute of Environmental Science, Szent István University, Páter Károly u. 1, 2100, Gödöllő, Hungary

^b Department of Physical and Applied Geology, Eötvös Loránd University, Pázmány Péter sétány 1/C, 1117, Budapest, Hungary

^c Department of Atomic Physics, Eötvös University, Pázmány Péter sétány 1/A, 1117, Budapest, Hungary

^d Lithosphere Fluid Research Laboratory, Department of Petrology and Geochemistry, Eötvös University, Pázmány Péter sétány 1/C, 1117, Budapest, Hungary

ARTICLE INFO

Article history:

Received 11 February 2016

Received in revised form

6 June 2016

Accepted 11 July 2016

Available online 1 August 2016

Keywords:

GIS

Geogenic radiation

Mapping

ABSTRACT

A detailed ambient gamma dose equivalent rate mapping based on field measurements at ground level and at 1 m height was carried out at 142 sites in 80 × 90 km area in Pest County, Hungary. Detailed digital image processing analysis was carried out to identify and characterise spatial features such as outlying points, anomalous zones and linear edges in a smoothed TIN interpolated surface. The applied method proceeds from the simple shaded relief model and digital cross-sections to the more complex gradient magnitude and gradient direction maps, 2nd derivative profile curvature map, relief map and lineament density map. Each map is analysed for statistical characteristics and histogram-based image segmentation is used to delineate areas homogeneous with respect to the parameter values in these maps. Assessment of spatial anisotropy is implemented by 2D autocorrelogram and directional variogram analyses. The identified spatial features are related to underlying geological and tectonic conditions using GIS technology. Results show that detailed digital image processing is efficient in revealing the pattern present in field-measured ambient gamma dose equivalent rates and they are related to regional scale tectonic zones and surface sedimentary lithological conditions in the study area.

© 2016 Elsevier Ltd. All rights reserved.

1. Introduction

Ambient gamma dose equivalent rate originate from artificial and natural radiation. The artificial radiation is caused by nuclear weapon tests, nuclear reactor fall-outs during normal operation and medical works (UNSCEAR, 2000). Natural outdoor gamma radiation originates from cosmic rays and from the decay of radionuclides present in the air, on the ground surface (e.g. radon daughter products deposited during rain storms) and in the soil (e.g. U and Th series) (UNSCEAR, 2000).

There are two major sources of natural background gamma radiation in the outdoor environment (NERMS, 2014):

- (1) Cosmic gamma radiation originates from outside the Solar System and accounts for about 50% of the annual external

absorbed dose. This source is partly screened by the Earth's magnetic field and the atmosphere. They may produce showers of secondary particles that penetrate and impact the Earth's atmosphere and sometimes even reach the surface.

- (2) Terrestrial gamma radiation consists primarily of radiation from the natural decay chain of uranium (²³⁵U and ²³⁸U), thorium (²³²Th) and potassium (⁴⁰K) and accounts for about 50% of the annual external absorbed dose. Additionally, radon (²²²Rn, ²²⁰Rn and their short-lived progeny) is an important source of natural gamma radioactivity in air, too. The isotopes ²²²Rn and ²²⁰Rn originate from the ²³⁸U and ²³²Th series, respectively. Especially ²²²Rn will be transported through the atmosphere after exhalation from the soil. The contribution to the gamma radiation dose in air from ²²²Rn and its progenies is small (0.5 (nSv/h)/(Bq/m³, for EEC concentration, equilibrium factor is 0.5), but after precipitation events when significant amounts of progeny are deposited on the ground, significant temporary rises of gamma dose rate occur that could easily double or triple the background radiation dose during an hour or more (Smetsers

* Corresponding author.

E-mail addresses: sz_k_zs@yahoo.de (K.Z. Szabó), petrik.atus@gmail.com (A. Petrik), akos@ludens.elte.hu (Á. Horváth), cszabo@elte.hu (C. Szabó).

and Blaauboer, 1997; Horng and Jianga, 2004; Inomata et al., 2007, Bossew et al., 2016). Radon exhalation is affected by rock and soil layers down to a few meters. However, several studies have shown that a lot of phenomena can affect radon upward movement e.g. the presence of faults or tectonic zones, the karst systems. These phenomena can enhance the radon exhalation from deeper layers which can be the source of elevated gamma dose rate, even as in the proximity of uranium mineralizations (Nezmal et al., 1991; Kemski et al., 1992; Ioannides et al., 2003; Swakon et al., 2005; Pereira and Neves, 2010; Vaupotič et al., 2010). Several studies observed close relationship of soil and rock uranium concentration, gamma dose rate, soil gas radon concentration and indoor radon concentration (Barnet et al., 2005; Barnet and Fojtíková, 2008; Minda et al., 2009; Duarte et al., 2011; García-Talavera et al., 2013). Szegvary et al. (2007) found that terrestrial gamma dose rate is a good estimator for radon flux from ground. One part of the ongoing project of the Radioactivity Environmental Monitoring (REM) Group (European Commission, Joint Research Centre) on European Atlas of Natural Radiation (EANR) is the European Geogenic Radon Map (EGRM). The aim of this map is to display “what earth delivers” in terms of radon. Candidate quantities for this map are ones which are independent of anthropogenic factors that influence indoor radon concentrations strongly (such as building styles and living habits) and are constant over a geological timescale (Gruber et al., 2013). Candidates are radon concentration in soil gas, permeability and combinations of them, or “proxies” such as geochemical

quantities or the terrestrial gamma dose (De Cort et al., 2011; Gruber et al., 2013; Cinelli et al., 2014, 2015). There are several methods to build a geogenic radon potential (GRP) map. In the first version of the EGRM, geological units were classified according to the so called Nezmal-RP, which takes into account soil gas Rn concentration and permeability (Gruber et al., 2013; Szabó et al., 2014). The map was a geological map in which geological units were coded according to the mean radon potential. To improve the first version of the EGRM it was proposed to take into account other radon related quantities, such as the terrestrial gamma dose rate (Gruber et al., 2013; Cinelli et al., 2014; Bossew et al., 2016). Pasculli et al. (2014) used geographical weighted regression (GWR) in order to build a radon potential map including directly and, as far as possible, in a quantitative way the geological features of the selected territory. In order to compile a geogenic radon potential (GRP) map for a model area in Central-Hungary, spatial auxiliary information (soil, geology, topography, land use and climate) representing GRP forming environmental factors were taken into account to support the spatial inference of the locally measured GRP values (Pásztor et al., 2016).

Outdoor radiation levels are usually expressed in terms of ambient dose equivalent rate at 10 mm depth on the ICRU 30 cm diameter tissue-equivalent sphere, $H^*(10)$ (International Commission on Radiation Units and Measurements, ICRU, 1993). $H^*(10)$ is commonly abbreviated to ambient dose rate, measured in Sv (Sievert). The average ambient dose equivalent rate for the period

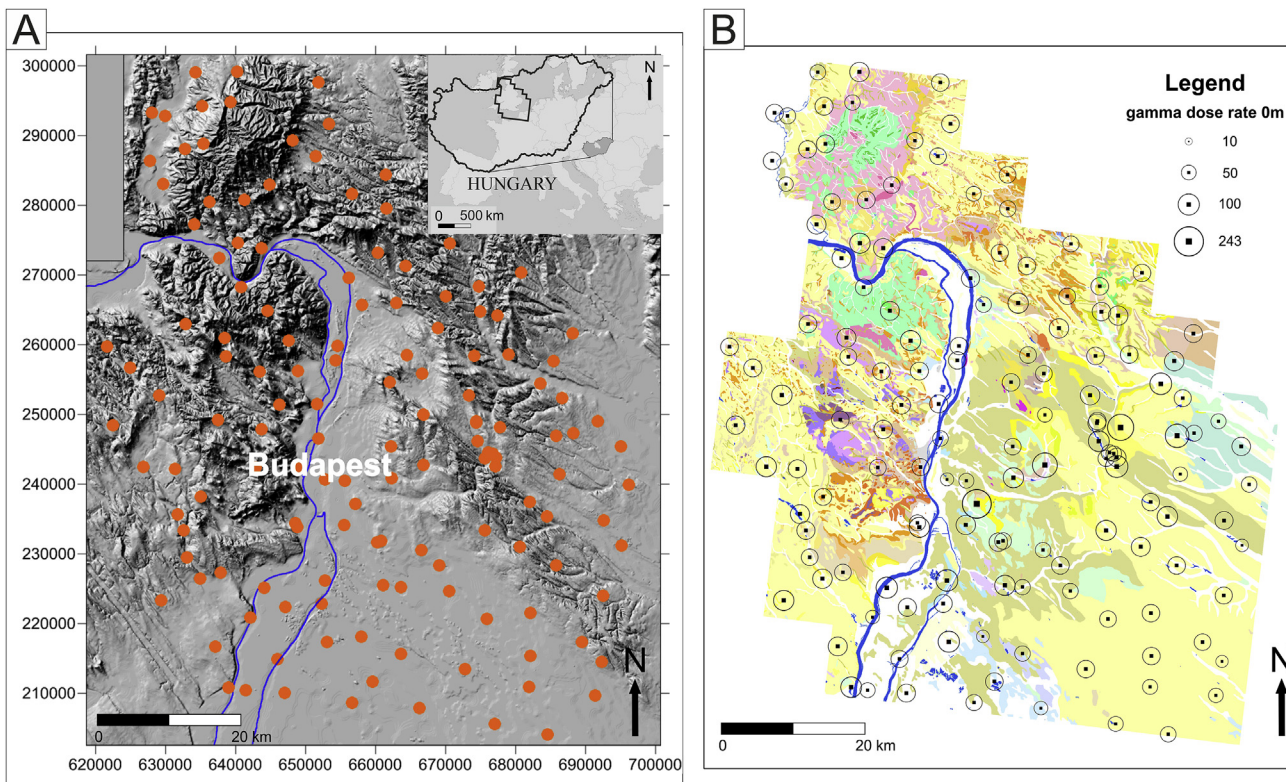


Fig. 1. Study area. A. Shaded relief map of the study area showing Budapest capital city and River Danube (blue line). Solid dot: location of gamma dose rate measurement sites. Inset: Irregular polygon shows the location of the study area. B. Simplified geology map. Purple and pink: Mesozoic sedimentary rocks. Light and dark green: Tertiary volcanic rocks. Light and dark orange: Tertiary sedimentary rocks. Yellow, beige, grey and blue are Quaternary sediments. The radius of the empty circles is proportional to the ambient gamma dose equivalent rate values (nSv/h) at the measurement sites. (For interpretation of the references to colour in this figure legend, the reader is referred to the web version of this article.)

2005–2013 at the 96 Hungarian National Measurement Sites is between 58 and 161 nSv/h (NERMS, 2014).

The objective of this study is to investigate the relationship of field-measured ambient gamma dose equivalent rate to the geological structures by means of spatial pattern analysis using digital image processing through the example of a regional scale radiation mapping dataset.

2. Study area

The study area is located in the Pannonian Basin and includes Budapest and the majority of Pest County (Fig. 1). The 80 × 90 km study area encompasses 5400 km² covering 6.5% of the country. This part of Hungary has the highest population density. Twenty-eight percent (2.73 million) of the population of the country (9.9 million) live in the 220 settlements of the study area. The area is also characterized by diverse geological background, thus providing excellent conditions for geogenic gamma dose rate mapping and spatial distribution research. The northernmost part of the study area comprises andesite and dacite over the Tertiary sedimentary basin covering the Paleozoic crystalline basement (Fig. 1B) (Gyalog, 1996). Besides Mesozoic carbonates (limestone, dolomite and marl), a great variety of Tertiary rock formations including Eocene and Oligocene limestone, marl and sandstone, Miocene clay and limestone and Pliocene clay, sand and gravel are found in the area. The Mesozoic and Paleozoic strata of the Pest Plane and Gödöllő Hills is covered by several hundred meters Miocene, Pliocene, Pleistocene and Holocene sediments such as sand, drift sand, gravel, loess, marl, silt, clay or limestone (Gyalog, 1996). The geological units in the hilly areas are meshed with recent or paleo-rivers providing Quaternary fluvial sediment in the valleys of the mountains, in addition to alluvial plain (mud and sand) at larger streams. The topographic elevation ranges between 938 m in the hilly northeast (Cserhát Mts. and Gödöllő Hills) and 100 m asl. in the Pest Plain in the middle.

3. Materials and methods

3.1. Field measurement

Ambient gamma dose equivalent rate ($H^*(10)$) (Sv) was measured by an FH 40 G-L10 portable instrument (manufactured by Thermo Fisher Scientific Inc.) incorporating an energy-filtered proportional gamma detector. Its measuring range is 10–100 nSv/h, energy range is 30 keV–4.4 MeV. Gamma dose rates were measured at the surface (0 m data series) and at a distance of 1 m above the surface (1 m data series). For each location 3–5 measurements spanning over 2 min were carried out and these measurements were then averaged to a single value. Thus, the single measurement taken at each location took 6–10 min.

The gamma dose rate measurement was a part of a complex geogenic radon mapping study, thus the bases of the site selection were the spatial extension of geological formations and the distribution of settlements (built-up areas). The internationally suggested 10 × 10 km² grid for the European indoor radon map (Dubois et al., 2010; Tollefsen et al., 2011) helped to achieve a spatially uniform sample distribution. On average, three measurement sites were taken in each cell, which resulted in 3.2 km average distance to the nearest neighbours among the 142 measurement sites. The three dominating geological formations were selected in each cell and a measurement in each formation was made, also taking the locality of the settlements into account. Thus, the sampling scheme is similar to a stratified (grid-based) random sampling. Geographic coordinates for the 142 measurement sites were

determined by a 5 m resolution GPS device.

Measurements were performed from May 2010 to December 2011. Seasonality did not have an influence on the measured values: according to the Kruskal-Wallis Test the medians of the outlier free data in different months are the same at the 95% confidence level ($p = 0.34$) (Kruskal and Wallis, 1952).

3.2. Statistical analysis

Summary statistics used in this study include measures of central tendency and variability. These statistics are the minimum, lower quartile, median, upper quartile, maximum and average (arithmetic mean), mode, standard deviation, median absolute

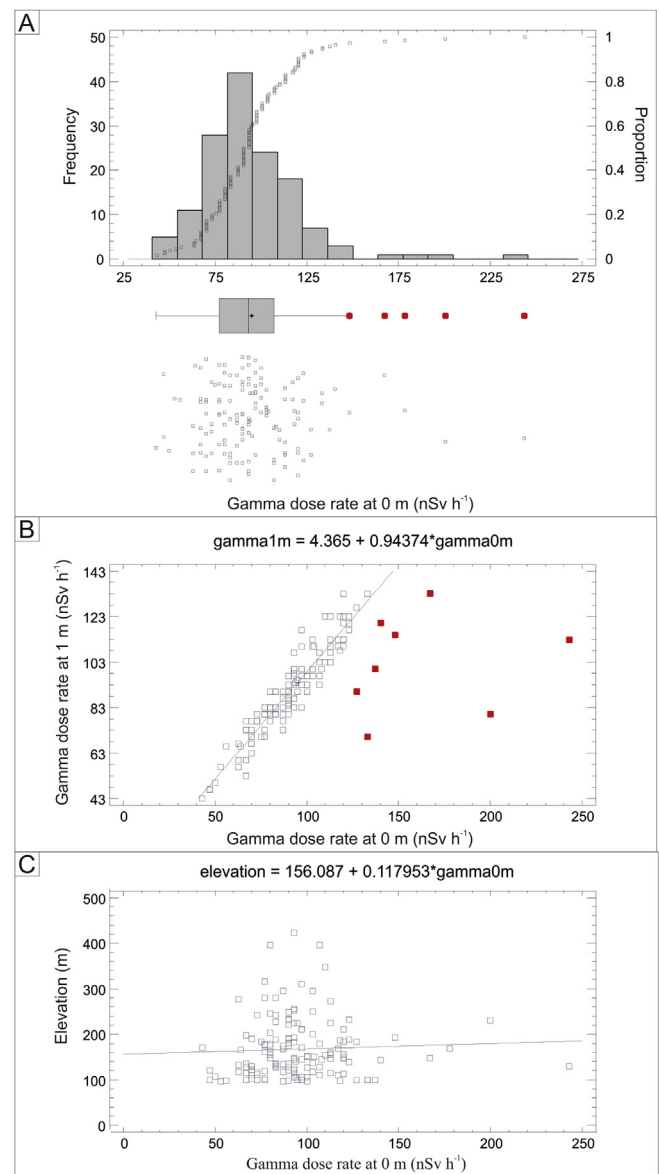


Fig. 2. Statistical analysis of gamma dose rates measured in the field ($n = 142$). A. Univariate distribution analysis at the 0 m heights: empirical histogram; box plot showing the univariate outliers as solid red dots and scatterplot. B. Bivariate regression analysis between gamma dose rate at 0 m and 1 m above the surface. Solid red dots indicate bivariate outliers. C. Bivariate regression analysis between the measured gamma dose rate and the topographic altitude. Note the lack of relationship. (For interpretation of the references to colour in this figure legend, the reader is referred to the web version of this article.)

deviation (MAD), range and inter-quartile range. Tukey's (1977) inner-fence criteria were used for outlier (anomalous gamma dose rate value) definition.

Simple least-squares linear regression analysis with additive constant was performed to explore the linear relationship between the gamma dose rate at different heights (0 m and 1 m above the surface). Strength of relationship is expressed by the Pearson's linear correlation coefficient r (Rodgers and Nicewander, 1988). All of the statistical tests applied in this study were significant at the 95% confidence level.

3.3. Mapping and spatial analysis

Field-measured gamma dose rate was plotted on maps to observe their spatial distribution. On the map in Fig. 1B circles indicate the measurement sites and the radius of the circle is linearly proportional to the gamma dose rate value.

Spatial analysis in this study is based on a continuous gamma dose rate surface interpolated from the 142 measurement points using the linear and accurate Triangular Irregular Network (TIN) interpolation method (Guibas and Stolfi, 1985). Grid size of 250 m was used based on the shortest distance between the closest two measurement sites. Successive moving average smoothing was applied to generalize the TIN model and to suppress small elements and to enhance large-scale significant features of gamma dose rate distribution in the study area. First, a series of 5×5 , 13×13 , 17×17 , 21×21 , 31×31 and 41×41 window size moving average low-pass

filter smoothing was applied to the original 250 m spaced TIN map. The TIN map smoothed with the 21×21 (5250×5250 m) window size revealed best the spatial trends and patterns without losing much detail and it was used for digital image processing such as edge detection and for other analyses such as spatial autocorrelation and directional variogram calculations. According to Evans (1972), the statistical properties of point attributes are more stable if the 2D interpolated data surface is smoothed before analysis, further supporting the use of smoothing before spatial analysis.

Error of interpolation was estimated by calculating the difference between the interpolated surface and the original data points. Results show that the applied smoothed TIN interpolation is a good model as the average error is -1.21 nSv/h, equal to a 1.3% relative error, with unbiased symmetric distribution. The t -test confirmed that the expected average error is zero at the 95% confidence level. The outlier data set has a lower average error of -0.75 nSv/h, equal to a 0.8% relative error. At the few outlier values in the main linear zone anomaly (see below) the error can be as high as -47 and 76 nSv/h which confirms the efficiency of the applied smoothing for regional trend pattern recovery.

A systematic digital image processing methodology is applied to image segmentation and image enhancement of the interpolated gamma dose rate field measurements according to Evans (1972) method as extended by Jordan (2007). This method, originally developed for digital elevation models, proceed from simple univariate data display and evaluation, through edge detection and image segmentation, to the multivariate interpretation of results

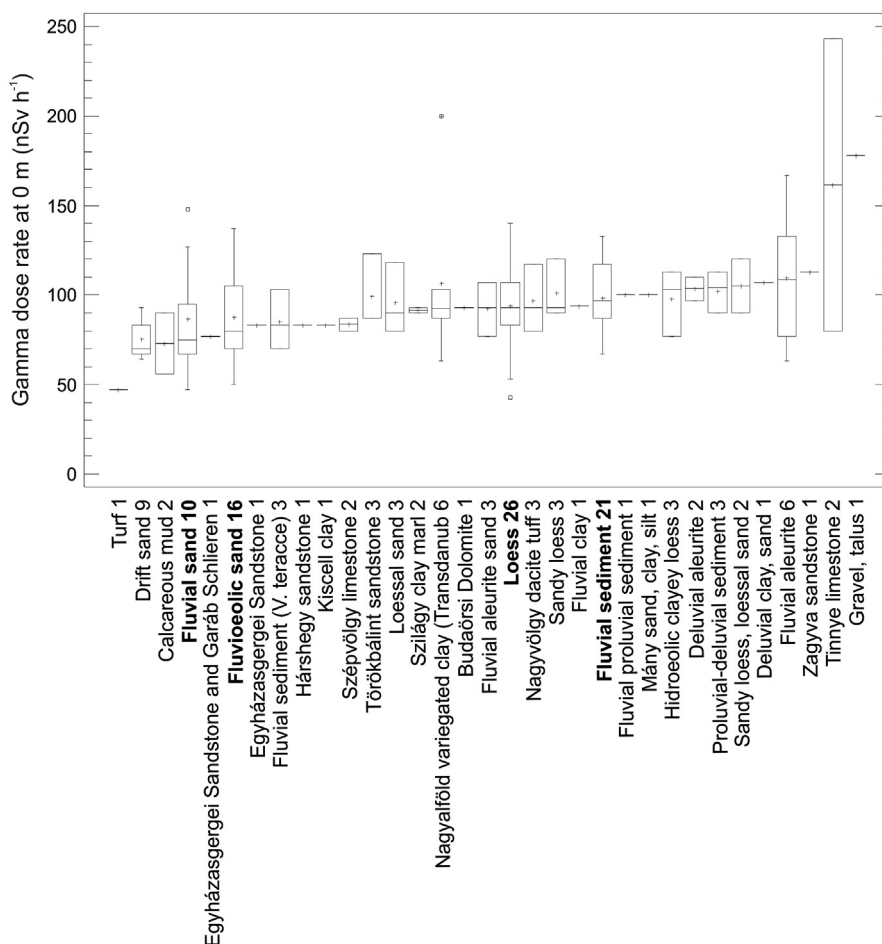


Fig. 3. Box and whisker diagram of gamma dose rate measured at 0 m for different geological formations, arranged in decreasing order of median values. Figures show the number of measurement sites for each geological formation. Bold indicates geological formations with more than 8 samples. See text for details.

using GIS technology. First, the investigated smoothed TIN-interpolated gamma dose rate map is displayed as a shaded relief surface (see Fig. 4A and B) and contour map (see Fig. 4A) for visual

pattern recognition. In this study the shaded relief model was a key component because it was the most suitable data display for the recognition and interpretation of complex 2D patterns related to

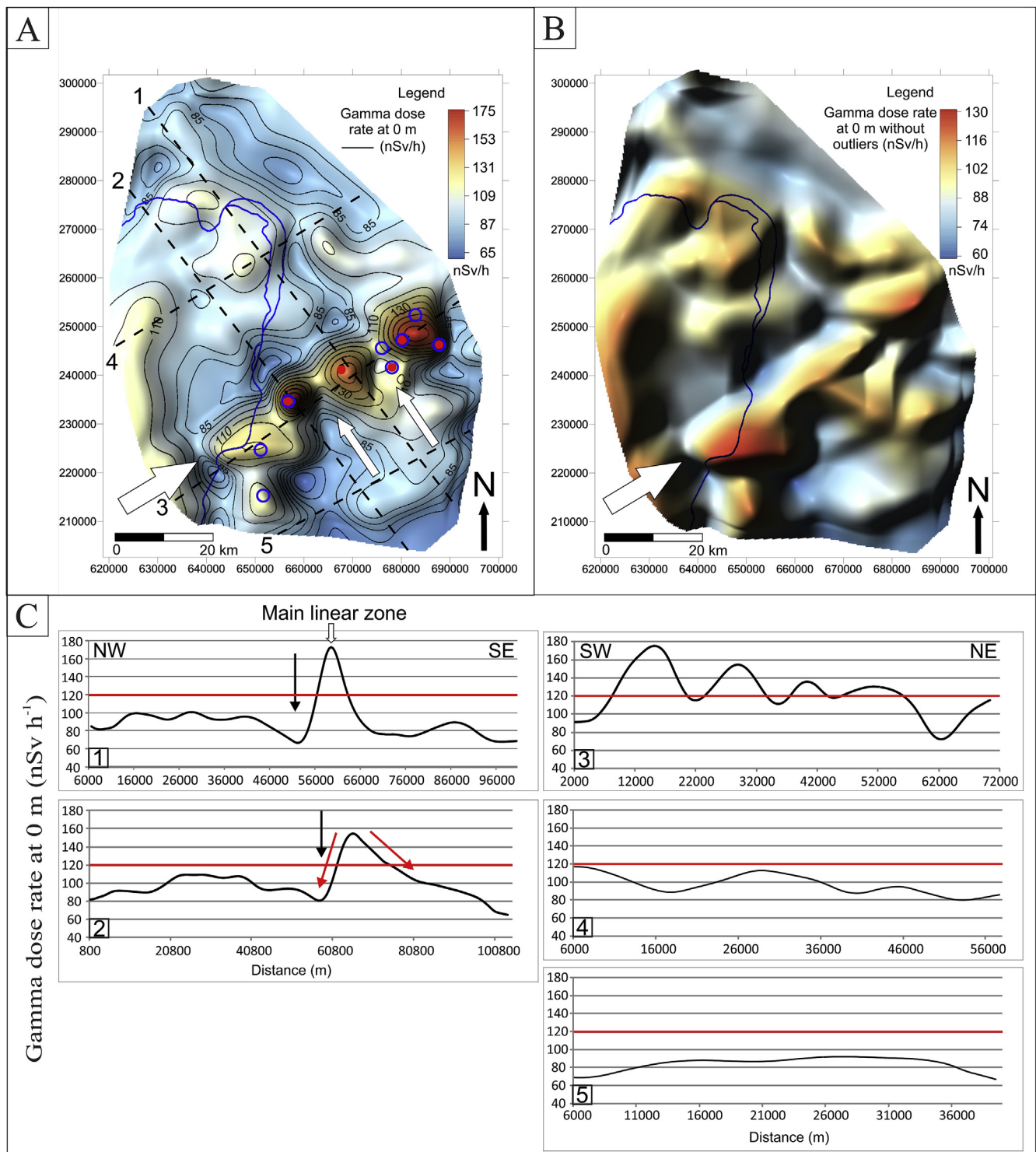


Fig. 4. Smoothed TIN surface display of measured gamma dose rates. A. Composite image of the colour coded gamma dose rate map and the shaded relief map calculated from smoothed TIN surface model of the gamma dose rate measured at the surface (0 m), smoothed with a 21×21 (5250 \times 5250 m) window size moving average low-pass filter. The contour lines are also overlaid. Solid red dots: statistically identified univariate outliers. Blue empty circles: statistically identified bivariate outliers. Arrows highlight linear features (see text for details). Dashed lines show the location of the digital cross-sections in Fig. 4A. B. The same map as in Fig. 4A but without the outliers. Note that the SW-NE main linear zone of anomaly, emphasized with heavy white arrow, remains a prominent feature without the outliers. Blue line indicated River Danube. C: Digital cross-sections (1–5) calculate from the smoothed TIN surface model. Locations of cross-sections are shown in Fig. 4A. (For interpretation of the references to colour in this figure legend, the reader is referred to the web version of this article.)

gamma dose rate distribution defined by the underlying geology. Eight shaded relief models were calculated at an azimuth interval of 45° and constant insolation inclination of 45° . The models used Lambertian reflection method and ten-time vertical exaggeration.

Five digital cross-sections were made across the study area (see Fig. 4C) in directions perpendicular to the main spatial feature anomaly (see below in Section 4.2. Mapping and spatial analysis) in order to study the local conditions at prominent features.

The difference between the highest and the lowest gamma dose rate values divided by the median value in a moving window (relative variation) applied to the original point data (142 measurement sites) was used to calculate the relief map. The window size was increased from 100×100 m to $10,000 \times 10,000$ m (ca. one quarter of the study area). The final window size was defined by visual inspection when the most distinct homogeneous areas resulted (see Fig. 5).

Empirical directional variograms were calculated to capture anisotropy in the gamma dose rates in the study area. In addition to the variogram analysis, a 2D autocorrelogram was also made to reveal anisotropy present in the spatial gamma dose rate data.

Next, singular points are identified such as local minima, maxima and flats which can correspond to low and high gamma anomalies and uniform horizontal areas, respectively. The localization of surface-specific points, i.e. local maxima (peaks), minima (pits), saddle points (passes), flats and slope-breaks is fundamental in digital spatial analysis (Peucker and Douglas, 1975; Takahashi et al., 1995; Jordan, 2007). Peaks and pits were calculated using simple 'higher than' algorithms (Garbrecht and Martz, 1995). The gradient magnitude ('slope') and direction ('aspect') and curvatures were calculated for regular points only. Profile curvature, which is the 2nd derivative in the gradient direction, was used to identify areas with sudden changes and inflection lines between convex

and concave areas. If these lines are linear, it may suggest geological or tectonic control on the spatial pattern of geogenic gamma radiation.

The 2D gamma dose rate surface gradient magnitude (slope) and gradient direction (aspect) calculations used the unweighted eight-point numerical differentiation method (Prewitt operators) for its smoothing effect as implemented by the ILWIS 3.8 software.

In order to improve classification of gradient direction (aspect) data based on the histogram, the aspect histogram curves were smoothed with a five-point median filter (Tukey, 1977) to remove the systematic error shown as pikes at values of 45° azimuth due to numerical derivation over a rectangular grid (Jordan, 2003). In order to capture areas of uniform gradient direction value the classified map was post-processed with a 500×500 m majority filter (see Fig. 8B).

Sub-population identification followed the 'natural break' histogram slicing method. Digital map data such as gradient or curvature values were separated where the cumulative distribution function (CDF) had an inflection point (natural break) identified visually on the cumulative distribution plot. This point corresponds to a local minimum in the frequency histogram (multi-modal histogram, see Fig. 8C). The hence identified classes of the mapped parameters were displayed as homogeneous areas in the classified parameter maps.

Significant linear features, associated with sudden changes in the gamma dose rate map, defined by sharp grey-scale edges in the processed digital maps such as shaded relief model or sharp boundaries in the classified parameter maps such as the gradient, gradient direction and profile curvature maps were digitized on screen. The orientation of the obtained lineaments was compared to the regional lithological boundaries and tectonic lines using simple GIS map overlay. Lineament density map was also created by means of calculating the total length of lineaments within aggregation cells. Several window-sizes from 50×50 m to $5,000 \times 5,000$ m were tested for moving average smooth to find the best compromise between noise removal and keeping information detail. The 500×500 m cell size delivered the most spatial information in this case. The obtained density map was smoothed using a simple moving average smooth at the end to increase visual interpretability (see Fig. 10B).

Finally, verification of digital spatial data processing and data analysis results was carried out and all the digital maps were compared to detailed geological maps using GIS overlay. Spatial modelling was performed with Surfer 10, ILWIS 3.8 and ArcGIS 10 applications.

4. Results

4.1. Statistical analysis

According to the empirical histograms, gamma dose rate (measured either at the surface or at 1 m above the surface) has a homogeneous unimodal statistical distribution containing a few outliers. Gamma dose rate at the surface has a minimum 43 nSv/h, a maximum 243 nSv/h, an average 95 nSv/h (median 93 nSv/h) with a standard deviation 27 nSv/h (relative variability is 28%) (Fig. 2). The five high outliers above 148 nSv/h are located along a SW-NE line across the study area (Fig. 2A and 4A). Gamma dose rate at 1 m above the surface has a minimum 43 nSv/h, a maximum 133 nSv/h, an average 90 nSv/h (median 90 nSv/h) with a standard deviation 19 nSv/h (relative variability is 21%). Three low and three high outliers exist in data below 47 nSv/h and above 132 nSv/h, respectively. Difference of gamma dose rate measured at the surface and 1 m above the surface has a minimum 13 nSv/h, a maximum 20 nSv/h, an average 1 nSv/h (median 0 nSv/h) and a

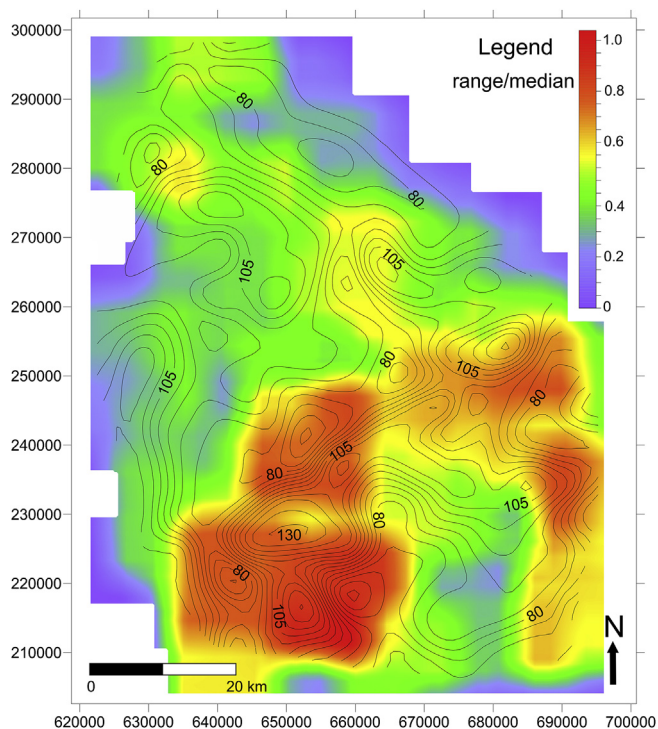


Fig. 5. Relief map calculated in a 71×71 grid cell ($17,750 \times 17,750$ m) moving window for the outlier free smoothed TIN surface as the ratio of gamma radiation value range and the median value within the window. Note that the high relief (high relative variation) concentrates in the main linear zone. Contour lines show gamma dose rates from the smoothed TIN map.

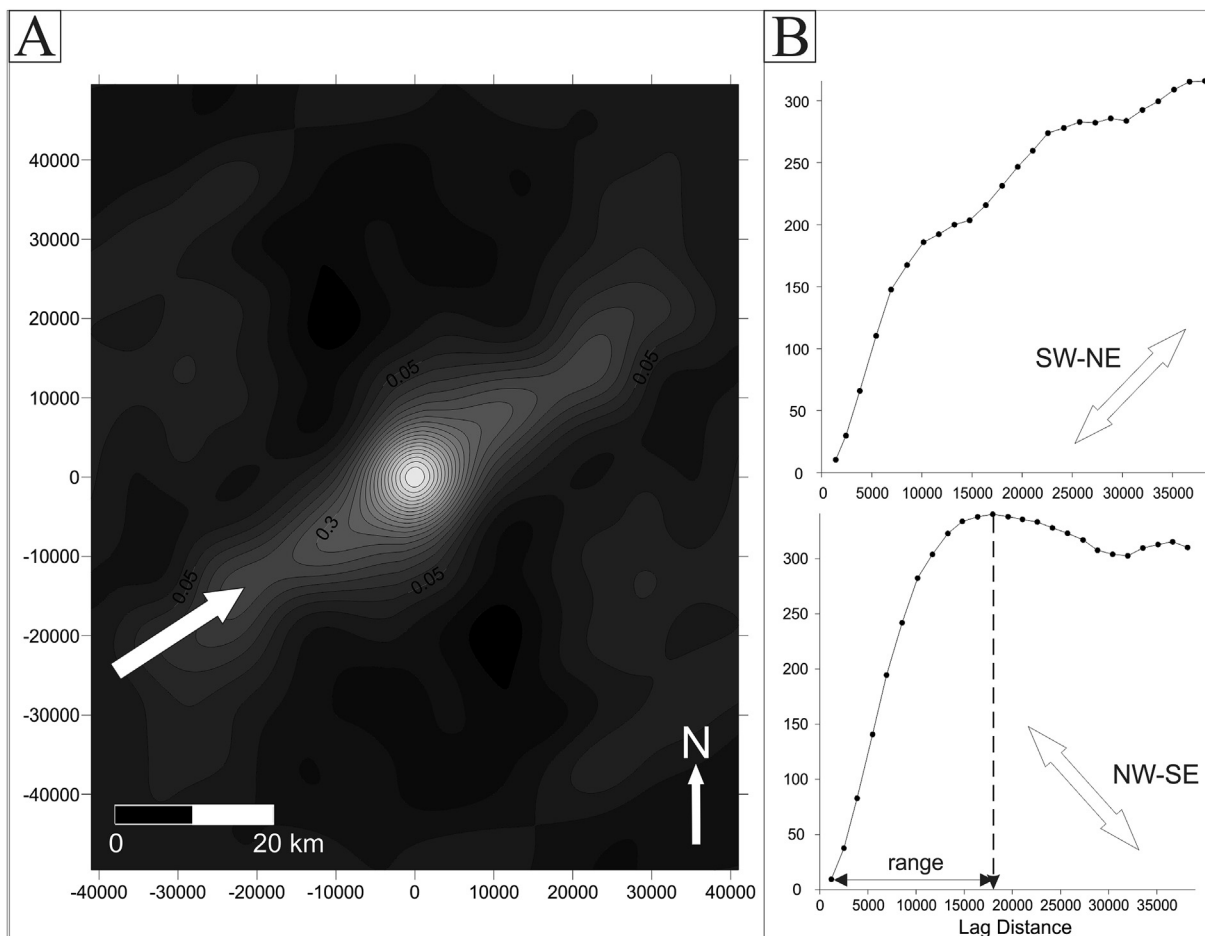


Fig. 6. Spatial autocorrelation analyses. A. Autocorrelogram for the gamma dose rate calculated from the smoothed TIN surface map. Contour lines show Pearson's correlation coefficient. Note the strong SE-NW anisotropy parallel to the main linear zone emphasized by the white arrow (Fig. 4). Coordinates are in meters. B. Directional variogram calculated from the smoothed TIN surface map in SW-NE direction (azimuth 45°, tolerance 30°) and in the perpendicular SE-NW direction (azimuth 150°, tolerance 30°).

standard deviation 6 nSv/h, excluding the 8 outlying different values. This shows that there is a negligible difference between the two datasets obtained at different measurement heights. The Kolmogorov-Smirnov test (homogeneity of cumulative distributions) and the Kruskal-Wallis test (homogeneity of medians) confirmed the homogeneity of the two outlier-free datasets at the 95% confidence level.

Simple bivariate regression analysis between gamma dose rate at 0 m and 1 m above the surface shows significant linear relationship with correlation coefficient of 0.95, excluding the eight bivariate outlying samples (Fig. 2B). All of the bivariate outliers are located along a SW-NE line across the study area (Fig. 4A). At the eight outlying sites the gamma dose rate is higher at the surface than at 1 m above the surface. Due to the insignificant difference between the gamma dose rates measured at the two different heights, also taking into account that this study focuses on the immediate effect of terrestrial earth materials (soil and rock), mapping and spatial analysis is presented in this paper only for the gamma dose rate measured at 0 m.

Finally, bivariate regression analysis shows no relationship between the measured gamma dose rate and the topographic altitude (Fig. 2C).

The 142 measurement sites belong to 33 different geological formations based on the 1:100,000 digital Geological Map of Hungary (Fig. 1B). Values of gamma dose rates measured on different geological formations were plotted in a box and whiskers

diagram (Fig. 3). There are only 5 geological formations which have more than 8 sample points (bold lettered formations in Fig. 3), which is a criterion for the Mann-Whitney homogeneity test. However, there is now significant difference between their medians, except for drift sand and fluvial sediment. Still, it can be seen in the figure that the median of gamma dose rates of these formations is in increasing order from drift sand (70 nSv h⁻¹) to fluvial sand (75 nSv h⁻¹), fluvioeolic sand (80 nSv h⁻¹), loess (93 nSv h⁻¹) and to fluvial sediment (97 nSv h⁻¹). This is a similar order that was obtained for soil gas radon activity concentration in the study area (Szabó et al., 2014).

4.2. Mapping and spatial analysis

The smallest grid cell that resolves all measurement points for the interpolated gamma dose rate surface is defined by the two closest points located 249 m apart from each other. The 21 × 21 (5250 × 5250 m) window size moving average (low-pass) filter was used to smooth the 250 m resolution TIN-interpolated surface grid of the gamma dose rate (measured at 0 m height). Fig. 4A and B show the interpolated surfaces for all data and for data without the statistical outliers, respectively. A clear SW-NE elevated gamma dose rate zone emerges as a 'ridge' in the smoothed TIN map (heavy white arrow in Fig. 4A). This main linear zone is present even if the outliers along this SW-NE zone are excluded (Fig. 4B). It is apparent that this zone has a sharp edge on the northern side while it is

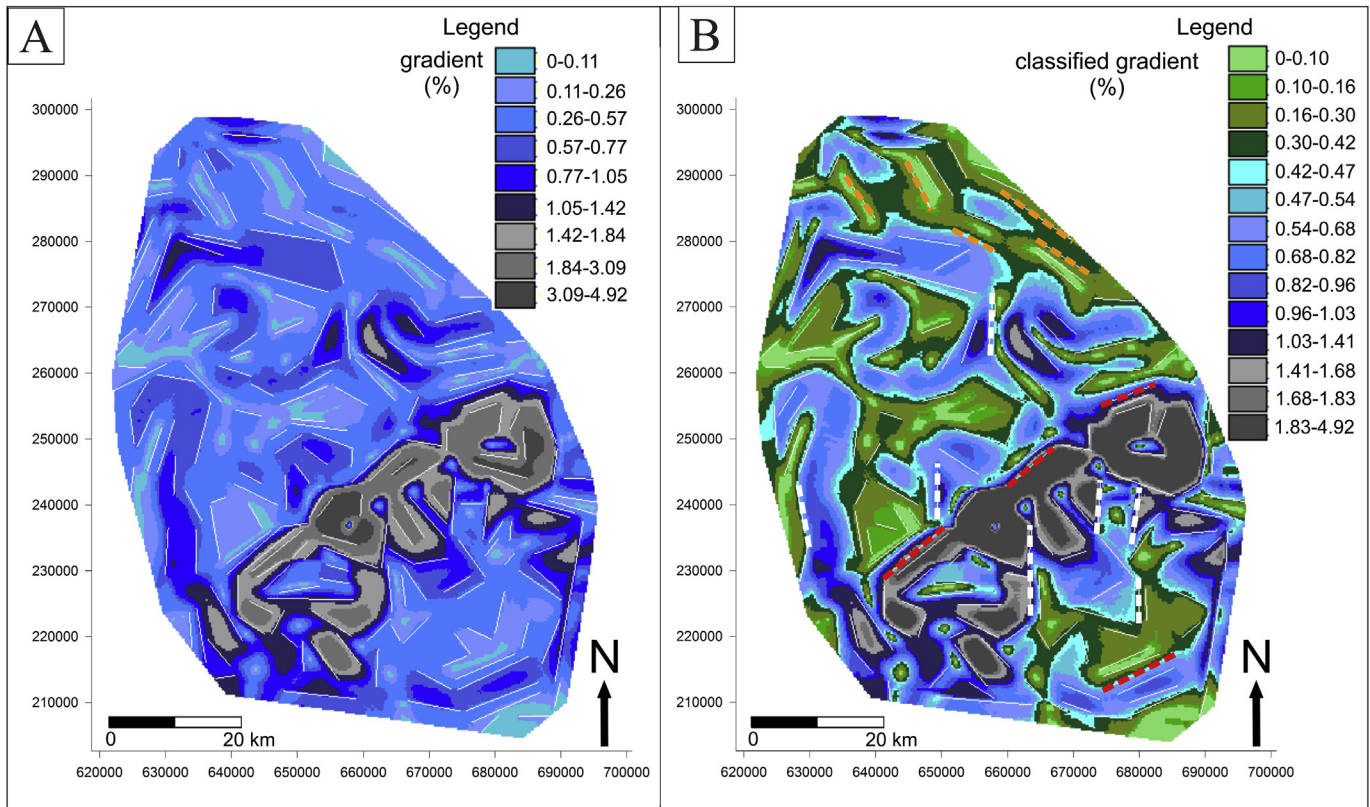


Fig. 7. Gradient map for gamma dose rates. A. Colour scale gradient map (in units of percent). White lines are linear edges identified in this map. B. Classified gradient map. Linear edges at class boundaries are identified as lineaments shown by lines. Note that various colours of the lines correspond to the three prevailing directions: SW-NE (red), N-S (white) and SE-NW (orange). (For interpretation of the references to colour in this figure legend, the reader is referred to the web version of this article.)

irregular to the south. Another prominent feature is the SE-NW oriented linear feature of low values appearing as a ‘valley’ cross-cutting the whole area including the main linear zone anomaly (light white arrows in Fig. 4A). The regions to the north and to the south of the main linear zone are characterized by irregular gamma dose rate pattern.

The two digital cross-sections perpendicular to the main linear zone also display the elevated gamma dose rates relative to its surrounding in this zone (cross-sections 1 and 2 in Fig. 4C). In cross-section 2 in Fig. 4C the asymmetry of the main linear zone is the most apparent having a higher decreasing gradient on the northerly side (red arrows). These two cross-sections also reveal that the sharp northern linear edge of the main linear zone is a zone of local minima in the same SW-NE direction. An obvious characteristic in these cross-sections is the uniform constant gamma dose rate levels in the surrounding regions on the both sides of the main linear zone as shown by the red line corresponding to a maximum value (120 nSv/h) in the surrounding regions.

Digital cross-section along the main linear zone across the local maxima (statistically identified outlying values) shows the uniformity of the gamma dose rates within the zone, on the average (cross-section 3 in Fig. 4C). Digital cross-sections parallel to the main linear zone in the areas on its both sides also display the overall uniform gamma dose rate levels in these surrounding regions (cross-sections 4 and 5 in Fig. 4C).

The relief map calculated in a 71×71 grid cell ($17,750 \times 17,750$ m) moving window for the outlier free smoothed TIN surface was enhanced for visual interpretation using a 21×21 grid cell moving average smooth. The relief map shows that the measured gamma dose rate values have the highest variability in

the main linear zone (Fig. 5). Also, the northern side of the main anomaly zone appears more regular than in the south.

The two-dimensional autocorrelation calculated for the smoothed TIN surface shows strong spatial autocorrelation of gamma dose rate in the SW-NE direction parallel to the main linear zone (Fig. 6A). The strong SW-NE direction anisotropy is also captured by the directional variograms parallel to and perpendicular to the main linear zone (azimuth: 45° and 150° , respectively, with 30° tolerance) (Fig. 6B and C). The variogram in the SW-NE direction has no defined range (trend effect) (Fig. 6B), whereas the variogram in the SE-NW direction has a well-defined range (Fig. 6C) which confirms the strong anisotropy in the gamma dose rates in the study area.

The 2D gradient map shows the magnitude of gamma dose rate change in the gradient direction. High values indicate large changes in unit distance. Fig. 7A shows that the gamma dose rate gradient is the highest in the main linear zone and it is higher on the northern side of the zone, whereas it is less steep towards the south (Fig. 7A). When the gradient map is classified based on the histogram slicing method, the boundaries of the slope classes appear as linear edges (Fig. 7B). Moreover, these linear edges are arranged in three main orientations in the SW-NE, SE-NW and the N-S directions.

The calculated gradient direction map in various grayscale shading is shown in Fig. 8A. The histogram of the gradient direction ranging from 0 to 360° displays significant multimodality (peaks) corresponding to pixels facing the same direction (Fig. 8C). When the histogram of the gradient direction is sliced into classes according to the peaks and these classes are displayed in a map with various colours the SW-NE main linear zone readily emerges (Fig. 8B). Just like in the classified gradient map (Fig. 7B), edges are

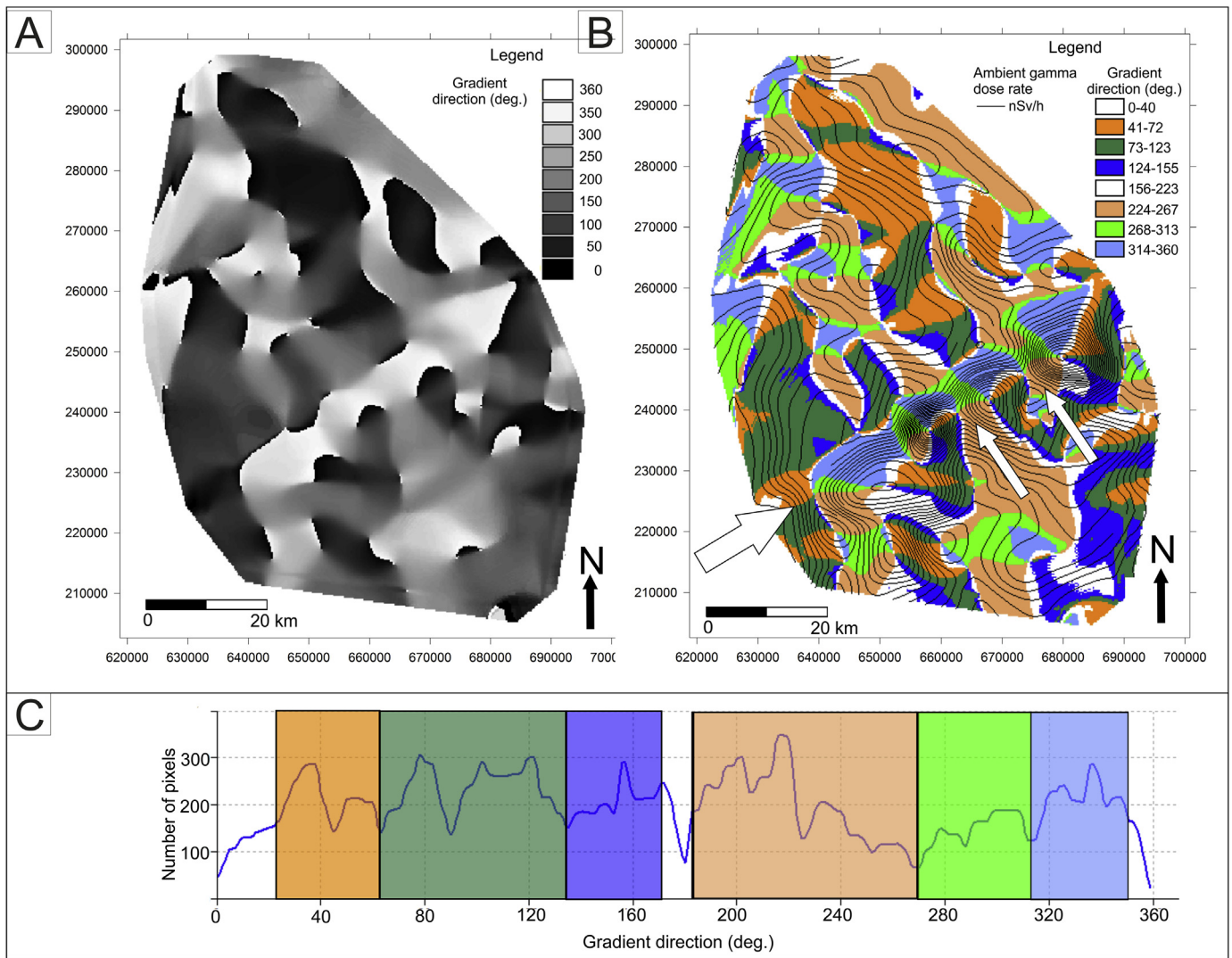


Fig. 8. Gradient direction analysis. A. Gradient direction map in greyscale shading. B. Classified gradient direction map. Classes correspond to the sliced histogram in Fig. 8C. Linear edges at class boundaries are identified as lineaments shown by lines. Note that various colours correspond to the three prevailing directions: SW-NE (blue), N-S (green) and SE-NW (orange). Heavy arrow shows the SW-NE main linear zone. Light arrows highlight the SE-NW dissecting zones. The zero degree (0°) direction is to the north. (For interpretation of the references to colour in this figure legend, the reader is referred to the web version of this article.)

linear and have three main directions (SW-NE, SE-NW and the N-S directions). It is obvious in the classified gradient direction map that the main linear zone is dissected by perpendicular SE-NW equally spaced zones. In these dissecting zones the gamma dose rate values are lower relative to the rest of the main linear zone as seen in Fig. 4A.

The second derivative calculated in the gradient direction is the profile curvature and it shows the change in the gradient. Sudden changes in gamma dose rate (high profile curvature values) are located along the main linear zone (Fig. 9A). This zone shows up as a series of high negative curvature (convex) areas corresponding to the SW-NE oriented gamma dose rate anomaly (heavy arrow in Fig. 9A). It is more interesting that this feature is bounded by a narrow linear low gamma zone of high positive curvature (concave) values appearing as a 'valley' in the gamma dose rate map to the north (light arrow in Fig. 9A). Fig. 9B shows the profile curvature map classified based on its sliced histogram for the outlier free dataset. In this figure the SW-NE oriented main linear zone clearly emerges as a distinct feature bounded by a sharp linear edge to the north whereas it is irregular to the south. This model delineates

unambiguously the narrow linear low gamma zone to the north of the main linear anomaly zone (Fig. 9B).

Finally, all significant linear edges (lineaments) in the previous maps were manually digitized as lineaments and their spatial distribution was displayed in a rose diagram. According to the lineament length rose diagram, there are three major directions: SW-NE, SE-NW and N-S (Fig. 10A). The highest dispersion in the lineament orientation is associated with the northerly (N-S) direction. In general, the high dispersion of lineament orientation is characteristic to this dataset. The lineament density map in Fig. 10B shows that linear edges are focused in the main linear zone.

5. Discussion

The results of the statistical analysis show that there is no significant difference between the gamma dose rate measured at the surface (0 m height) and 1 m above the surface. The overall values in the study area (average 90 nSv/h) are not different from the national average gamma dose rate range (58–161 nSv/h) (NERMS, 2014). Outlier values (148–243 nSv/h) are systematically found in

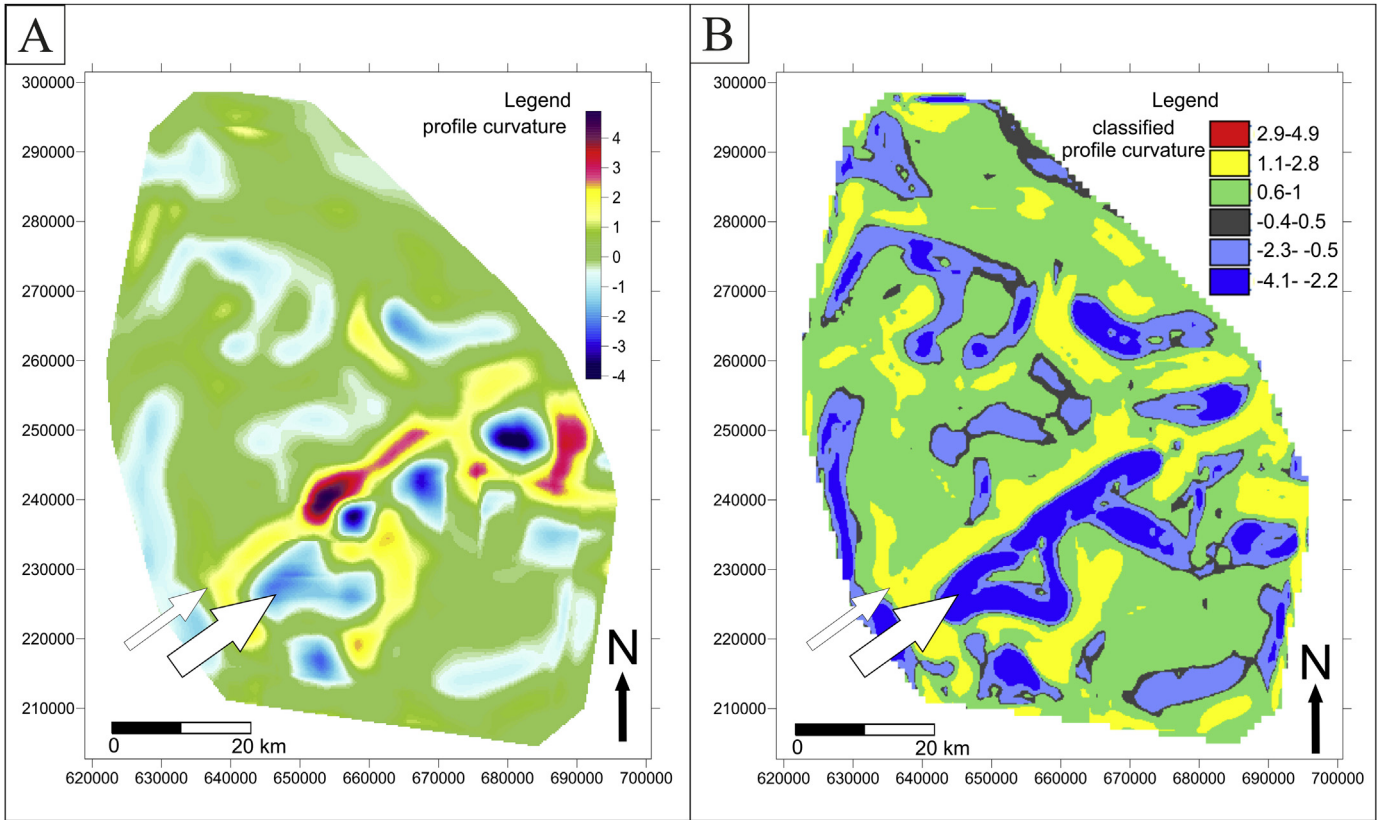


Fig. 9. Profile curvature for gamma dose rate map. A. Colour scale profile curvature map. Heavy and light white arrows indicate the main linear and the low gamma dose rate zones, respectively. B. Classified profile curvature map. Heavy and light arrows indicate the main linear and the low gamma dose rate zones, respectively. (For interpretation of the references to colour in this figure legend, the reader is referred to the web version of this article.)

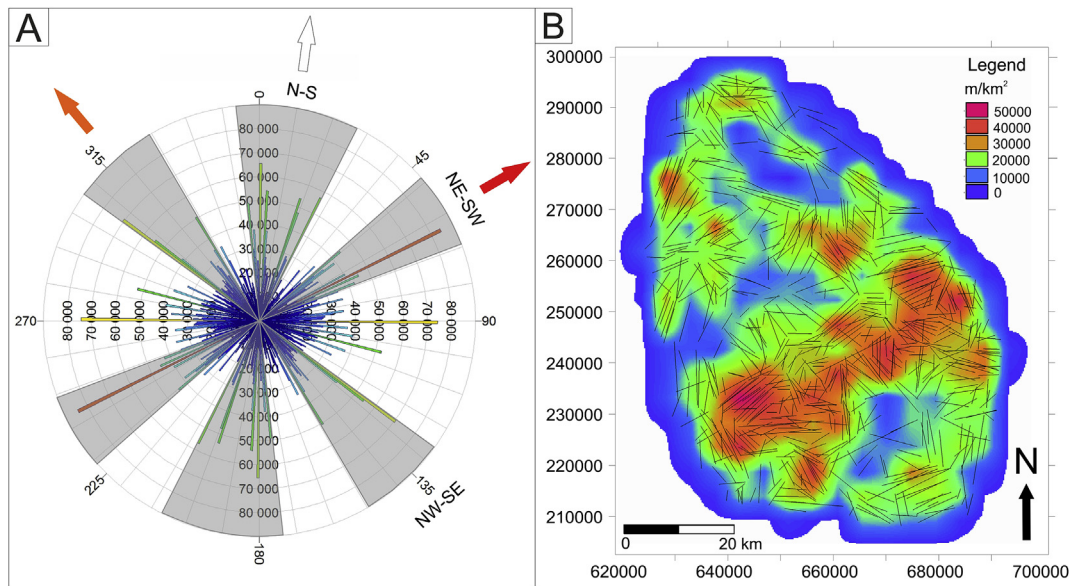


Fig. 10. Lineament analysis. A. Lineament length rose diagram showing the direction and length distribution of lineaments in Fig. 10B. Grey shading emphasises the three main directions. Note the high dispersion of lineament orientation. Various colours of arrows correspond to the three prevailing directions: SW-NE (red), N-S (white) and SE-NW (orange). B. Lineament map (black lines) overlaid by the colour scale lineament density map. Note that most of the linear edges (lineaments) concentrate along the SW-NE main linear zone. See text for details. (For interpretation of the references to colour in this figure legend, the reader is referred to the web version of this article.)

the main linear zone of elevated gamma dose rate. For data interpretation the topographic altitude is not considered a significant factor because bivariate analysis showed no relationship between

the measured gamma dose rate and the topographic altitude for the whole area.

The Mid Hungarian Shear Zone (MHSZ) is transecting the study

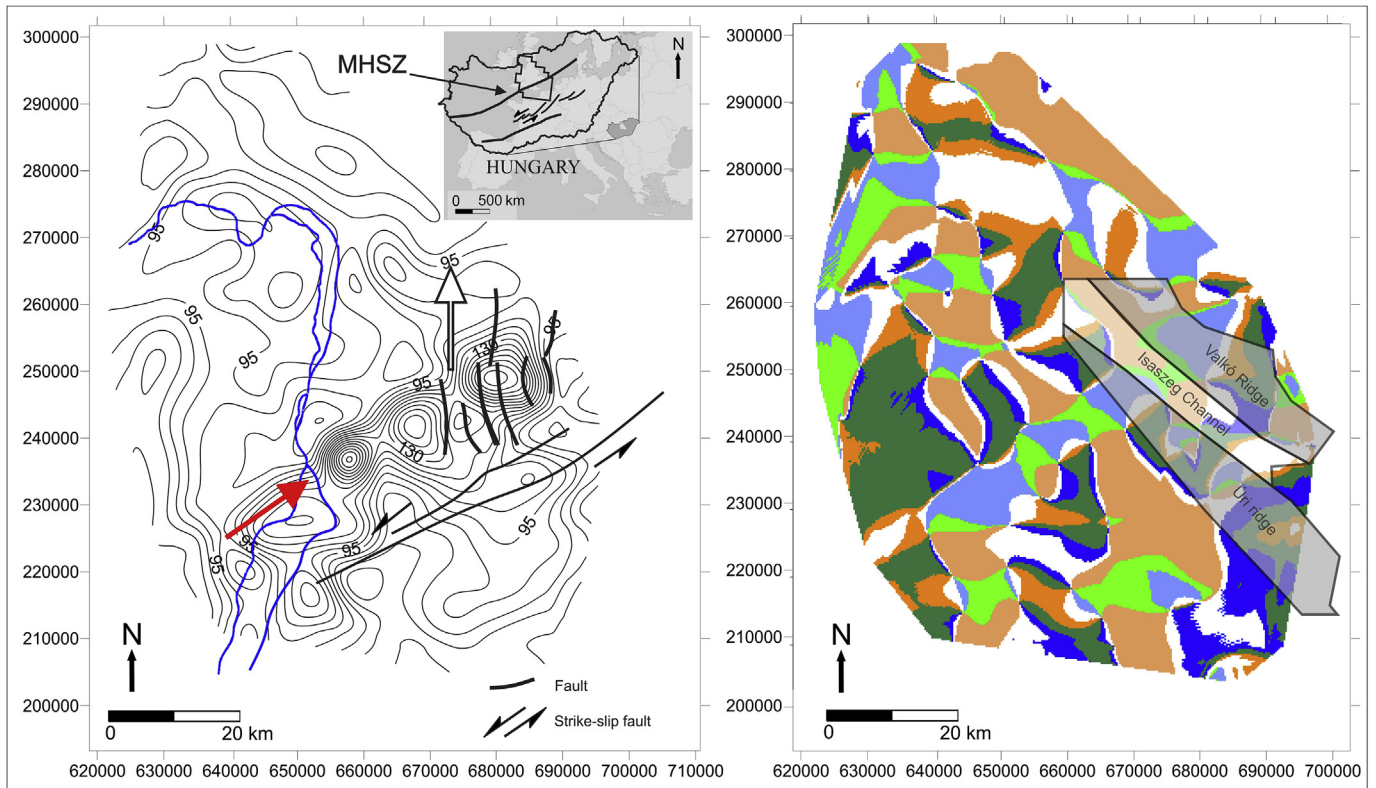


Fig. 11. Interpretation of geogenic gamma dose rate spatial features. A. Tectonic map (Ruszkiczay-Rüdiger et al., 2007) overlaid by gamma dose rate contour lines. Red arrow emphasises the SW-NE main linear zone and the parallel prevailing direction of identified linear edges. Note that the zone is parallel to the major tectonic displacement zone. White arrow emphasises the N-S oriented linear edges, which are parallel to normal faults. Inset: Irregular polygon shows the location of the study area. Main regional tectonic lines are also shown. B. Classified gradient direction map overlaid by the geological map of the sediment-filled SE-NW running valleys and thin sediment covered ridges. Note that the location of the valleys coincides with low gamma dose rate swaths transecting the main linear zone. See text for details. (For interpretation of the references to colour in this figure legend, the reader is referred to the web version of this article.)

area in the middle (Fig. 11A). Detailed tectonic mapping evidences that there is a major strike-slip fault zone in the SW-NE direction in the studied area coinciding with the main linear gamma anomaly zone identified in this study. It is obvious in Fig. 11A and from the presented detailed digital spatial data analysis that the main linear zone in the measured gamma dose rates is spatially related to the MHSZ fault system in the study area. Geological control on the SW-NE main linear zone is evidenced by the identified spatial features of the study area: the main anomaly zone has an elongated shape, it is sub-parallel to the transecting geological shear zone, its spatial location coincides with the shear zone and it has sharp edges. Also, the identified outlier gamma values align in the fault zone. According to previous geological investigation, the major horizontal displacement fault zone (MHSZ) is associated with a parallel running series of N-S normal faults (Ruszkiczay-Rüdiger et al., 2007) (Fig. 11A). Fig. 11A shows that the main linear zone of gamma dose rate is in fact located over these N-S normal faults. The N-S edges (lineaments) in the gamma dose rate revealed in this study are most probably associated with this N-S running fault system.

Finally, the identified SE-NW gamma dose rate spatial features are parallel to the main morphological land forms such as valleys and ridges prevailing in the study area (Fig. 11B). The above presented digital spatial data analysis, the classified gradient direction map in particular (Fig. 8B), has shown that the major linear anomaly zone is dissected by perpendicular SE-NW equally spaced low gamma zones. These low gamma zones are associated with the sediment-filled valleys covered by eolian sand and drift sand (Ruszkiczay-Rüdiger et al., 2009). The ridges, where relatively

higher gamma dose rate values are found, are covered mostly by thinner loess and fine sandy loess with several paleosol horizons (Ruszkiczay-Rüdiger et al., 2009). Szabó et al. (2014) has shown that the eolian sand and drift sand in the topographic valleys have less geogenic radiation than the loess and sand found in the ridges. These sedimentary and geogenic radiation conditions readily explain the SE-NW spatial features transecting the main linear zone (Fig. 11B). According to the recent EU Directive on Ionizing Radiation (Council Directive, 2013/59/Euratom) Member States have to compile national radon maps and establish action plans to address the long-term risks from radon exposure. Results of this study can be used for geogenic radiation mapping both at the national and European levels since terrestrial gamma dose rate can be a predictor for the geogenic radon potential (De Cort et al., 2011; Gruber et al., 2013).

6. Conclusions

This study has shown that the applied digital image processing and spatial analysis methods can be used for the recognition and characterization of spatial pattern in field-measured ambient gamma dose equivalent rate. The simple but carefully designed linear TIN interpolation improved with a smoothing generalization has proved to be efficient to capture the main spatial features of gamma dose rate in the study area. This is readily visualized by the shaded relief model and cross-section displays of the data. According to the autocorrelation analysis, the prevailing feature in the study area is the SW-NE main linear gamma radiation anomaly zone containing the outlying high values. Based on the relief

calculation, this is the most variable area of gamma dose rates. For the identification of significant gamma value changes along linear edges (lineaments) the classified slope map and the second derivative profile curvature map were the most successful. The circular statistics (rose diagram) calculated from the lineament map revealed three major directions corresponding to geological structures such as fault zones and surface sediments associated with morphological valleys and ridges.

In conclusion, this study confirms that the main spatial features identified in the gamma dose rate map are influenced by the underlying geological conditions and surface sediment distribution defined by morphological conditions in the study area.

Acknowledgements

This research has been supported by the Hungarian National Scientific Research Foundation (OTKA project to K.Z. Szabó, No. PD115810). We acknowledge the support of the Kutató Kari Kiválósági Támogatás - Research Centre of Excellence - 9878-3/2016/FEKUT Fund. This paper reports on the research at the GEM-RG Geochemistry, Modelling and Decisions Research Group. This is the 83rd publication of the Lithosphere Fluid Research Laboratory (LRG) at Eötvös University and carried out in agreement between Eötvös University and Szent István University (TTK/3489/1/2016).

References

- Barnet, I., Fojtíková, I., 2008. Soil gas radon, indoor radon and gamma dose rate in CZ: contribution to geostatistical methods for European atlas of natural radiations. *Radiat. Prot. Dosim.* 130, 81–84.
- Barnet, I., Miksová, J., Fojtíková, I., 2005. Indoor – soil gas relationship in the central bohemian plutonic complex. *Ann. Geophys.* 48, 93–99.
- Bossew, P., Cinelli, G., Hernándeiz-Ceballos, M., Cernohlávek, N., Gruber, V., Dehandschutter, B., Menneson, F., Bleher, M., Stöhlker, U., Hellmann, I., Weiler, F., Tollefsen, T., Tognoli, P.V., de Cort, M., 2016. Estimating the terrestrial gamma dose rate by decomposition of the ambient dose equivalent rate. *J. Environ. Radioact.* (in press), <http://www.sciencedirect.com/science/article/pii/S0265931X16300364>.
- Cinelli, G., Hernándeiz-Ceballos, M.A., Bossew, P., Tollefsen, T., Sanchez, I., Marín-Ferrer, M., Nishev, A., Bogu_carskis, K., Gruber, V., De Cort, M., 2014. A method to estimate the terrestrial component of ambient dose equivalent rate from EURDEP Routine monitoring data to improve the European geogenic radon map. In: 12th International Workshop on the Geological Aspects of Radon Risk Mapping, Czech Geological Survey and Radon Vos, Prague. ISBN 978-80-01-05548-9, 45–50. JRC91086.
- Cinelli, G., Tollefsen, T., Bossew, P., Gruber, V., De Cort, M., 2015. The European atlas of natural radiation. In: Presentation, Conference Rad-2015, Budva (Montenegro), 8–12 June 2015. <http://www.rad2015.rad-conference.org/news.php> (section radon-thoron) (accessed 05.02.16.).
- De Cort, M., Gruber, V., Tollefsen, T., Bossew, P., Janssens, A., 2011. Towards a European atlas of natural radiation: goal, status and future perspectives. *Radio-protection* 46, 737–743.
- Duarte, P., Mateus, A., Paiva, I., Trindade, R., Santos, P., 2011. Usefulness of systematic in situ gamma-ray surveys in the radiometric characterization of natural systems with poorly contrasting geological features (examples from NE of Portugal). *Appl. Radiat. Isot.* 69, 463–474.
- Dubois, G., Bossew, P., Tollefsen, T., De Cort, M., 2010. First steps towards a European atlas of natural radiation: status of the European indoor radon map. *J. Environ. Radioact.* 101, 786–798.
- Evans, I.S., 1972. General geomorphometry, derivatives of altitude, and descriptive statistics. In: Chorley, R.J. (Ed.), *Spatial Analysis in Geomorphology*. Methuen, London, pp. 17–90.
- Garbrecht, J., Martz, L.W., 1995. Agricultural research service publication NAWQL 95-3. In: TOPAZ: an Automated Digital Landscape Analysis Tool for Topographic Evaluation, Drainage Identification, Watershed Segmentation and Subcatchment Parameterisation: TOPAZ User Manual. - U.S. Department of Agriculture, p. 110, 95-3.
- García-Talavera, M., García-Pérez, A., Rey, C., Ramos, L., 2013. Mapping radon-prone areas using radiation dose rate and geological information. *J. Radiol. Prot.* 33, 605–620.
- Gruber, V., Bossew, P., De Cort, M., Tollefsen, T., 2013. The European map of the geogenic radon potential. *J. Radiol. Prot.* 33 (1), 51–60.
- Guibas, L., Stolfi, J., 1985. Primitives for the manipulation of general subdivisions and the computation of Voronoi diagrams. *ACM Trans. Graph.* 4, 74–123.
- Gyalog, L. (Ed.), 1996. Signal Code of the Geological Maps and Short Description of the Stratigraphical Units I (In Hungarian). Geological Institute of Hungary, Budapest. Special Paper 187.
- Hornig, M., Jianga, S., 2004. In situ measurements of gamma-ray intensity from radon progeny in rainwater. *Radiat. Meas.* 38 (1), 23–30.
- Inomata, Y., Chiba, M., Igarashi, Y., Aoyama, M., Hirose, K., 2007. Seasonal and spatial variations of enhanced gamma ray dose rates derived from ²²²Rn progeny during precipitation in Japan. *Atmos. Environ.* 41 (37), 8043–8057.
- Ioannides, K., Papachristodoulou, C., Stamoulis, K., Karamanis, D., Pavlides, S., Chatzpetros, A., Karakala, E., 2003. Soil gas radon: a tool for exploring active fault zones. *Appl. Radiat. Isot.* 59, 205–213.
- Jordan, G., 2003. Morphometric analysis and tectonic interpretation of digital terrain data: a case study. *Earth Surf. Process. Landforms* 28, 807–822.
- Jordan, G., 2007. Digital terrain analysis in a GIS environment. Concepts and development. In: Peckham, R.J., Jordan, G. (Eds.), *Digital Terrain Modelling, Development and Applications in a Policy Support Environment*. Springer Verlag, Berlin, pp. 2–39.
- Kemski, J., Klingel, R., Schneiders, H., Siehl, A., Wiegand, J., 1992. Geological structure and geochemistry controlling radon in soil gas. *RPD* 45 (1–4), 235–239.
- Kruskal, W.H., Wallis, W.A., 1952. Use of ranks in one-criterion variance analysis. *J. Am. Stat. Assoc.* 47, 583–621.
- Minda, M., Tóth, G.Y., Horváth, I., Barnet, I., Hámori, K., Tóth, E., 2009. Indoor radon mapping and its relation to geology in Hungary. *Environ. Geol.* 57, 601–609.
- Neznal, M., Neznal, M., Smarda, J., 1991. Radon infiltration risk from the ground in Chaby, Prague. In: Barnet, I. (Ed.), *Radon Investigations in Czechoslovakia*, vol. 2. Czech Geological Survey, Prague, pp. 34–39.
- NERMS, 2014. OKSER 2013. Annual Report of the National Environmental Radiological Monitoring System, p. 86.
- Pasculli, A., Palermi, S., Sarra, A., Piacentini, T., Miccadei, E., 2014. A modelling methodology for the analysis of radon potential based on environmental geology and geographically weighted regression. *Env. Model. Soft.* 54, 165–181.
- Pásztor, L., Szabó, K.Z., Szatmári, G., Laborczí, A., Horváth, A., 2016. Mapping geogenic radon potential by regression kriging. *Sci. Tot. Env.* 544, 883–891.
- Pereira, A.J.S.C., Neves, L.J.P.F., 2010. Geogenic controls of indoor radon in Western Iberia. In: Barnet, I., Neznal, M., Pacherova, P. (Eds.), *Proc., 10th International Workshop on the Geological Aspects of Radon Risk Mapping*. Czech Geological Survey, Radon v.o.s., Prague 2010, ISBN 978-80-7075-754-3, pp. 205–210. <http://www.radon.eu/workshop2010/>.
- Peucker, T.K., Douglas, D.H., 1975. Detection of surface-specific points by local parallel processing of discrete terrain elevation data. *Comput. Graph. Image Process.* 4, 375–387.
- Rodgers, J.L., Nicewander, W.A., 1988. Thirteen ways to look at the correlation coefficient. *Am. Stat.* 42, 59–66.
- Ruszkiczay-Rüdiger, Z., Fodor, L., Horváth, E., Telbisz, T., 2009. Discrimination of fluvial, eolian and neotectonic features in a low hilly landscape: a DEM-based morphotectonic analysis in the Central Pannonian Basin, Hungary. *Geomorph* 104, 203–217.
- Ruszkiczay-Rüdiger, Z., Fodor, L., Horváth, E., 2007. Neotectonics and quaternary landscape evolution of the Gödöllő Hills, Central Pannonian Basin, Hungary. *Glob. Planet. Chang.* 58, 181–196.
- Smetters, R.C.G.M., Blaauboer, R.O., 1997. Source-dependent probability densities explaining frequency distributions of ambient dose rate in the Netherlands. *Radiat. Prot. Dosim.* 69, 33–42.
- Swakon, J., Kozak, K., Paszkowski, M., Gradzinski, R., Loskiewicz, J., Mazur, J., Janik, M., Bogacz, J., Horwacik, T., Olko, P., 2005. Radon concentration in soil gas around local disjunctive tectonic zones in the Krakow area. *J. Environ. Radioact.* 78, 137–149.
- Szabó, K.Z., Jordan, G., Horváth, Á., Szabó, C., 2014. Mapping the geogenic radon potential: methodology and spatial analysis for central Hungary. *J. Environ. Radioact.* 214, 74–83.
- Szegvary, T., Leuenberger, M.C., Conen, F., 2007. Predicting terrestrial ²²²Rn flux using gamma dose rate as a proxy. *Atmos. Chem. Phys.* 7, 2789–2795.
- Takahashi, S., Ikeda, T., Shinagawa, Y., Kunii, T.L., Ueda, M., 1995. Algorithms for extracting correct critical points and constructing topological graphs from discrete geographical elevation data. *Int. J. Eurogr. Assoc.* 14, 181–192.
- Tollefsen, T., Gruber, V., Bossew, P., De Cort, M., 2011. Status of the European indoor radon map. *Radiat. Prot. Dosim.* 145, 110–116.
- Tukey, J.W., 1977. *Exploratory Data Analysis*. Addison-Wesley.
- UNSCEAR Report, 2000. Sources and Effects of Ionising Radiation. UN, New York.
- Vaupotic, J., Gregoric, A., Kobal, I., Žvab, P., Kozak, K., Mazur, J., Kochowska, E., Grządziel, D., 2010. Radon concentration in soil gas and radon exhalation rate at the Ravne fault in NW Slovenia. *Nat. Hazards Earth Syst. Sci.* 10, 895–899.